CrossMark

Cost-effective wear and oxidation resistant electrodeposited Ni–pumice coating

S.T. Aruna [a,*], Shibayan Roy [b], Amit Sharma [c], G. Savitha [a], V.K. William Grips [a]

[a] Surface Engineering Division, Council of Scientific and Industrial Research-National Aerospace Laboratories, HAL Airport Road, Bangalore 560017, India
[b] Institut für Werkstoffwissenschaft und Werkstofftechnik, Chemnitz University of Technology, Erfenschlager Str. 73, 09125 Chemnitz, Germany
[c] Department of Materials Engineering, Indian Institute of Science, Bangalore 560 012, India

ABSTRACT

In the search for newer distributed phases that can be used in Ni-composite coatings, inexpensive and naturally available pumice has been identified as a potential candidate material. The composition of the pumice mineral as determined by Rietveld analysis shows the presence of corundum, quartz, mulllite, moganite and coesite phases. Pumice stone is crushed, ball-milled, dried and dispersed in a nickel sulfamate bath and Ni–pumice coatings are electrodeposited at different current densities and magnetic agitation speeds. Pumice particles are uniformly incorporated in the nickel matrix and Ni–pumice composite coatings with microhardness as high as 540 HK are obtained at the lowest applied current density. In the electrodeposited Ni–pumice coatings, the grain size of Ni increases with the applied current density. The overall intensity of texture development is slightly stronger for the Ni–pumice composite coating compared to plain Ni coating and the texture evolution is possibly not the strongest deciding factor for the enhanced properties of Ni–pumice coatings. The wear and oxidation resistances of Ni-pumice coating are commensurate with that of Ni-SiC coating electrodeposited under similar conditions.

© 2014 Elsevier B.V. All rights reserved.

1. Introduction

In recent years, there has been increased interest in the research and development of metal matrix composite coatings (MMCs) due to their expected engineering applications. These composite coatings can impart functional properties such as wear, corrosion and oxidation resistance, dispersion hardening or self-lubrication relative to pure metal, so that they can protect the metal substrates more effectively against severe environments during operation [1,2]. The properties of MMCs depend on the contributions from the distributed and matrix phases. They can be produced through a number of routes including metal processing, powder metallurgy, and electrodeposition techniques [2]. The codeposition of fine ceramic or polymer particles in a metal matrix can be achieved by an electrodeposition technique, which is a single step, low-temperature process that results in nanocomposite coatings wherein the matrix or the particles can be in nanosize or both can be in nanosize [3]. The nickel matrix prepared by electrodeposition has been widely used in the chemical, mechanical and electronic industries because of their wear, corrosion and oxidation resistance [3]. They find application as coatings of engine cylinders, high-pressure valves and dies and in the production of musical instruments, drill fittings, car accessories and small aircraft and electro-technical parts [4].

One of the continuing goals of the nanocomposite coatings is the production of economically viable coatings with enhanced properties such as higher microhardness and corrosion, oxidation and wear resistance. There are reports on the synthesis and properties of various composite coatings such as Ni–SiC, Ni–Si$_3$N$_4$, Ni–Al$_2$O$_3$, Ni–ZrO$_2$, Ni–CeO$_2$, Ni–TiO$_2$, Ni–La$_2$O$_3$, Ni–CNT, Ni–diamond and Ni–microcapsules [5–15]. Among these, Ni–SiC is the most widely used wear resistant composite coating on the trochoid of Wankel engines [6]. SiC powder is relatively expensive (15$ for 250 g) and its preparation involves multi-steps and high temperature calcinations. In the search for inexpensive and readily available ceramic particles, pumice stone seemed to be attractive.

Pumice stone is basically an alumino-silicate, has a Knoop hardness of 705, is very cheap (1$ for 250 g) and readily available and is actually a kind of glass [16]. It is used in precast masonry units, poured concrete, insulation and acoustic tile, and plaster. It is also used as an abrasive in polishes, pencil erasers, cosmetic exfoliants, toothpastes and the production of printed circuit boards. Pumice is a light, porous igneous volcanic rock. It has a porous structure and a large surface area and it can be processed easily [16]. The use of pumice as an adsorbent to remove metals from wastewater treatment at low cost is a well-established process. Pumice has been found to be effective for the removal of phosphate ions from water [18] and is used as an additive for cement [17]. However, there are no reports on the synthesis and properties of Ni composite coating containing pumice particles.

* Corresponding author. Tel.: +91 80 25086250; fax: +91 80 25210113.
E-mail addresses: aruna_reddy@nal.res.in, staruna194@gmail.com (S.T. Aruna).

The aim of this paper was to explore the potential application of naturally available pumice in the preparation of electrodeposited nickel metal matrix composites and evaluate the mechanical, wear and oxidation resistant properties of Ni–pumice coating. It was also aimed at comparing the properties with Ni–SiC coating, a commercial coating.

2. Experimental

2.1. Processing and characterization of pumice powder

Commercially available pumice stone (1$ for 250 g) was crushed using a pestle and mortar to get coarse powder. In order to further reduce the size of the particles, the coarse powder was subjected to ball milling (Fritsch Pulverisette) at 300 rpm for 5 h using tungsten carbide as the grinding media and ethanol as the solvent. The obtained gray colored powder was heat treated at 100 °C for 3 h to remove the moisture and was used for electrodeposition [19]. In order to identify the phases present in the pumice powder, the diffraction pattern was recorded using a powder X-ray diffractometer (Bruker D8-Advance) with CuK$_\alpha$ radiation source and scan speed of 0.5°/min. Crystallographic parameters were refined by XRD pattern and phase analysis was carried out using TOPAZ version 4.2 with inorganic crystal structure database (ICSD) [20]. The morphology of the pumice particles was determined using a field emission scanning electron microscope (FESEM-Carl Zeiss). The particle size distribution of the powder was measured using a Mastersizer 2000 particle size analyzer (Malvern instruments). The density of crushed pumice particles was determined by Archimedes' principle as follows: The powder was placed inside a pycnometer and was then filled with a fluid of known density, in which the powder was not soluble. The volume of the powder was determined by the difference between the volume as shown by the pycnometer, and the volume of liquid added (i.e. the volume of air displaced).

2.2. Preparation of Ni–pumice composite coating and its characterization

The composition of the nickel sulfamate plating bath and the parameters used for plating are summarized in Table 1. A pure nickel sheet (2.5 cm × 7.5 cm) and a brass substrate of the same dimension were used as anode and cathode respectively. The polished brass substrate of area 2.5 cm × 2.5 cm was degreased with acetone followed by cathodic cleaning and acid dipping and finally rinsed with distilled water. In order to ensure uniform dispersion of the powder, the electrolyte containing pumice particles was subjected to magnetic stirring (~600 rpm) for 15 h before the deposition process and during electrodeposition the particles were also magnetically stirred at different speeds. The electrodeposition was carried out on a brass substrate at room temperature by using an Aplab 7253 regulated DC power supply at various current densities (0.77, 1.55, 3.1 and 4.5 A dm^{-2} respectively

Table 1
Bath composition and deposition conditions used for Ni & Ni–pumice coating.

Bath composition	
Component	Concentration/g L^{-1}
Nickel sulfamate	300
Nickel chloride	10
Boric acid	30
Sodium lauryl sulfate	0.2
Pumice particles	100
Deposition conditions	
Parameters	Value
pH	4.0
Temperature/°C	25
Current density/A dm^{-2} (deposition time/min)	0.77 (360); 1.55 (180); 3.1 (90); 4.65 (45)
Magnetic stirring speed/rpm	300, 600, 900

for 6 h, 3 h, 1.5 h and 45 min at 300, 600 and 900 rpm). For oxidation studies, free-forms were prepared on stainless steel substrates at the optimized condition of 0.77 A dm^{-2} at 300 rpm for 48 h. The powder XRD patterns of Ni–pumice composite coatings electrodeposited at 0.77, 1.55, 3.1 and 4.65 A dm^{-2} at 300 rpm were also recorded using XRD (Bruker D-8 Advance system).

The surface images of Ni–pumice coatings were obtained by FESEM. In the present study, FESEM (Carl Zeiss SUPRA4OVP) equipped with GEMINI column and integrated with EBS/EBSD was used. For energy dispersive X-ray analysis (EDAX), 20 kV electron source was used and the interaction volume was approximately in the order of 3–4 μm and percentage error was under 1% (atomic). The working distance was 14.9 mm and conducting gold thickness was 10 nm and system volume was 5×10^{-5} mbar.

The cross-sectional metallographic specimens were prepared by sandwiching electrodeposited Ni–pumice coatings with a copper back-up in an epoxy followed by mechanical grinding and polishing with Al$_2$O$_3$ slurry, down to 0.3 μm. The microhardness measurements were performed on ten different locations on the cross-section of each coating (Micromet 2103, Buehler, 50 gf load). The cross-sectional optical micrographs of Ni–pumice coatings were recorded using a vertical metallurgical microscope. The area fraction of particles incorporated in the Ni matrix was calculated from the above optical microscope images using Image J analysis free software. The surface roughness of the coatings was measured using an atomic force microscope (AFM-Surface Imaging System).

The tribological performance of Ni and Ni–pumice composite coatings electrodeposited at 0.77 A dm^{-2} and 300 rpm for 6 h was investigated by conducting wear tests on a pin-on-disk tribometer (DUCOM, India) under ambient conditions of temperature and humidity (30 °C, 50% RH) at an applied load of 1 kg. More details regarding the wear studies have already been reported [21]. Similar experiments were repeated with the addition of commercial β-silicon carbide (M/s Xuzhou Jiechuang New Materials Technology Co. Ltd, China) particles. The Raman spectra of the wear tracks on the disks were recorded with a DILOR-JOBIN-YVON-SPEX (Paris, France) integrated Raman Spectrometer (Model LabRAM).

The global texture of plain Ni and Ni–pumice composite coatings electrodeposited at 0.77 A dm^{-2} and 300 rpm were measured by an XRD technique on the surfaces of the thick coatings. In this experimental measurement scheme, the normal direction to the measurement plane initially coincided with the diffraction vector. This is to say, the physical growth direction of the electrodeposited coatings initially lies parallel to the diffraction vector. Measurements were carried out using CuK$_\alpha$ radiation in a point detector mode. A texture goniometer based on Schulz reflection geometry (D8 Discover with GADDs, Bruker AXS, Germany) was used for texture measurement which operated in steps of χ = 5° and φ = 5°. Three incomplete pole figures, namely {111}, {200} and {311} were measured experimentally. Background correction was performed during texture measurement for each φ and χ positions. Quantitative texture analysis was carried out by calculating the orientation distribution functions (ODF) using LaboTex (LaboSoft s.c., Poland) software. Axial specimen symmetry was applied to symmetrize the texture data since coating materials are usually characterized by only one principal specimen direction (physical growth direction with respect to the substrate surface). Arbitrarily defined cell (ADC) algorithm was used and no restriction of specimen symmetry was imposed while calculating the ODFs.

In order to check the oxidation resistance of Ni, Ni–pumice and Ni–SiC coatings, the free forms electrodeposited at 0.77 A dm^{-2} and 300 rpm were heat treated at various temperatures in steps of 100 °C from 100 to 900 °C in air for 1 h. The heat treated samples were mounted in an epoxy, ground and polished. The microhardness measurements were carried out on the cross-sections and the average of 8 readings was reported. The isothermal oxidation experiments were carried out in air at 800 °C for 30 h. The mass measurements were

conducted after every 5 h using a balance with 0.01 mg sensitivity. The mass gain was mathematical average, which were obtained from duplicate specimens.

3. Results and discussion

3.1. Powder characterization

Fig. 1a and b shows the FESEM images of pumice and silicon carbide powders respectively. The pumice powder consisted of a mixture of smaller particles that were spherical in shape and some blocky angular shaped larger particles were also seen. Silicon carbide particles were irregular in shape (Fig. 1b). The average agglomerated particle size as determined by particle size analysis for the as crushed pumice powder was 23 μm which reduced to 6.69 μm upon ball-milling for 5 h (Fig. 2a). Silicon carbide powder was finer than pumice particles with an average agglomerated size of 1.82 μm (Fig. 2b) and showed a Gaussian distribution. Fig. 3 shows the Rietveld refined XRD pattern of ball-milled pumice powder. The quantitative analysis of the pumice powder showed 5 phases viz., corundum (4.641%), quartz low (10.976%), moganite (5.937%), mullite (33.267%) and coesite (45.179%). Corundum corresponds to α-alumina form with the chemical formula Al_2O_3 which crystallizes in trigonal crystal system. Moganite is a silicate mineral with the chemical formula SiO_2 which crystallizes in monoclinic crystal system. Mullite is a rare silicate mineral with the chemical formula $3Al_2O_3 \cdot 2SiO_2$ and crystallizes in orthorhombic crystal system. Coesite is a polymorph of SiO_2 with monoclinic crystal system that is formed when very high pressure (2–3 GPa) and moderately high temperature (700 °C) are applied to quartz. Quartz low phase corresponding
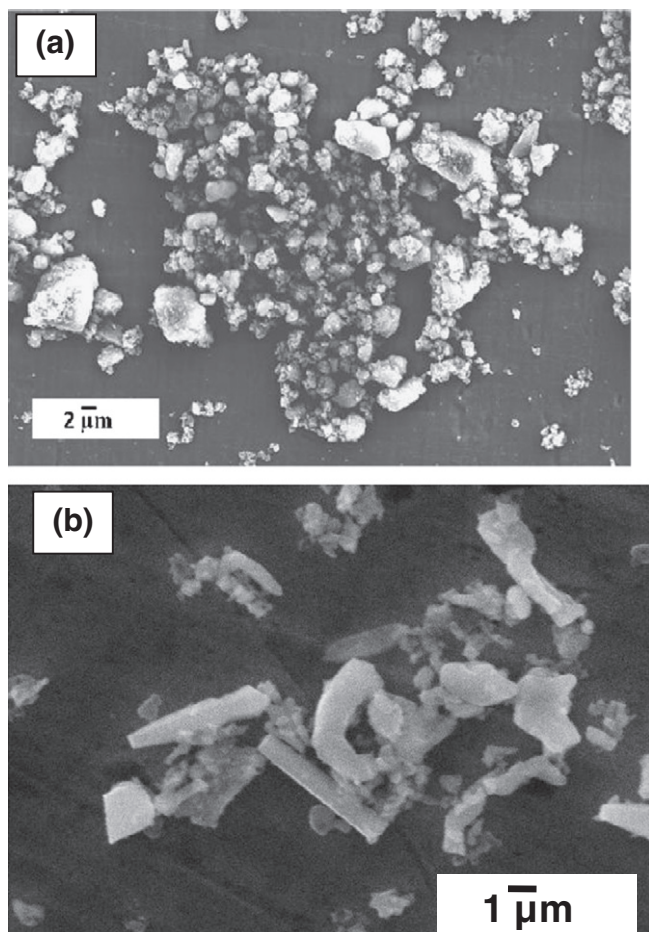

Fig. 1. FESEM images of (a) ball-milled pumice and (b) commercial SiC powders.
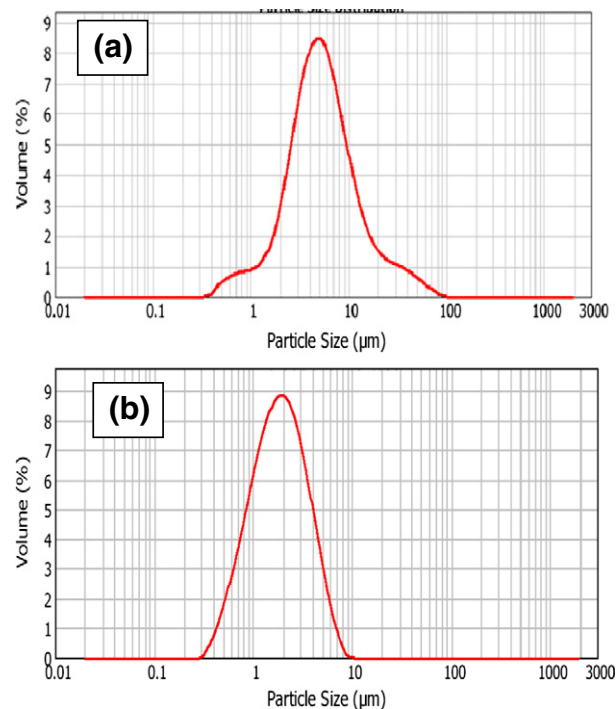

Fig. 2. Particle size distributions of (a) ball-milled pumice and (b) commercial SiC powders.

to silica crystallizes in trigonal system. Table 2 shows the values of Rietveld refined parameters of pumice powder. The XRD pattern of silicon carbide showed peaks corresponding to β-SiC phase (not shown) and a small trace of SiO_2. The crushed pumice particles had very low density (2.08 g cm^{-3} as determined by Archimedes' principle using pycnometer and xylene as the solvent).

3.2. Characterization of electrodeposited Ni–pumice composite coatings

3.2.1. XRD analysis of electrodeposited Ni–pumice coatings

Fig. 4 shows the XRD patterns of Ni–pumice coatings electrodeposited at different current densities and a magnetic agitation speed of 300 rpm. The average Ni grain size as determined by Scherrer's formula for Ni(111) and Ni(200) peaks increased with the current density. The Ni grain sizes were 12, 25, 30 and 32 nm respectively for the coatings electrodeposited at 0.77, 1.55, 3.1 and 4.65 A dm^{-2} at 300 rpm. Several authors [22,23] have also reported an increase of deposit's grain size with increasing current density. This has been attributed to the co-deposition of hydrogen at the cathode electrolyte interface. The changes in the surface energy and growth mechanisms in the presence of hydrogen are responsible for the increased crystallite size of deposits by increasing current density.

3.2.2. Microstructure, surface roughness, microhardness and tribological property of Ni–pumice composite coatings

Fig. 5 shows the cross-sectional optical micrographs of Ni–pumice composite coatings electrodeposited at various current densities and 300 rpm. It was evident from the images that at a given rpm, bigger particles were incorporated at lower current density. It was also observed that, irrespective of the current densities used for electrodeposition, bigger particles were incorporated in the nickel matrix at lower rpm and smaller particles were incorporated at higher rpm which corroborates well with our earlier work on Ni–Al_2O_3 coatings containing solution combustion and co-precipitation synthesized alumina powders [8]. At lower rpm, the bigger particles are not easily carried away from the cathode and as a result, the chance entrapment of bigger particles increases. The area fraction of particles incorporated in the nickel matrix
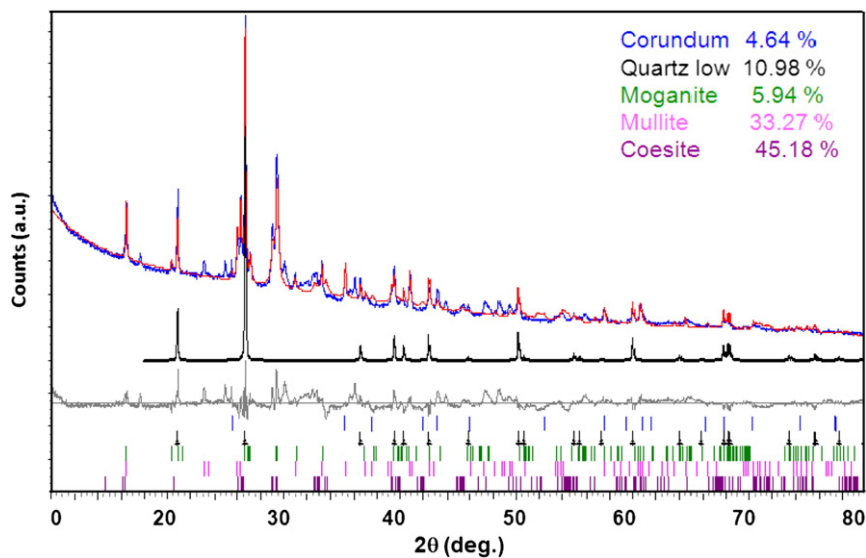
Fig. 3. The Rietveld refined XRD pattern of ball-milled pumice powder.

varied from 6 to 23% based on the current density and rpm. The area fraction of particles incorporated was the highest at the lowest applied current density and lowest stirring speed. The area fraction of particles incorporated in the Ni–pumice coatings electrodeposited at 0.77 A dm^{-2} was 23, 18 and 14% respectively at 300, 600 and 900 rpm. The area fraction of particles incorporated in the Ni–pumice coatings electrodeposited at 1.55 A dm^{-2} was 20, 15 and 10% respectively at 300, 600 and 900 rpm. The area fraction of particles incorporated in the Ni–pumice coatings electrodeposited at 3.1 A dm^{-2} was 18, 14 and 8% respectively at 300, 600 and 900 rpm. The area fraction of particles incorporated in the coatings electrodeposited at 4.65 A dm^{-2} was 12, 10 and 6% respectively at 300, 600 and 900 rpm.

Fig. 6a shows the FESEM image of the surface of electrodeposited Ni–pumice coating electrodeposited at 0.77 A dm^{-2} and 300 rpm. The surface of Ni–pumice exhibited dense and rough microstructure with a lot of nodules and the pumice particles were surrounding the nodules. In the case of Ni–SiC (Fig. 6b), the nodular features were not prevalent which may be attributed to the influence of irregular shape of SiC particles. Interestingly, a higher magnification FESEM image of few areas of Ni–pumice coating showed acicular crystalline structure with a crystallite size of ~100 nm (Fig. 6c & d). The EDAX data of these areas correspond to Ni rich areas. This feature may be attributed to the infiltration of nickel into the pores of pumice particles during electrodeposition. The EDAX data recorded on various spots on the surface of Ni–pumice coating (Fig. 6c & d) are tabulated in Table 3. From the EDAX data the following conclusions can be drawn: the dense features correspond to nickel phase and the porous features correspond to pumice phase.

The surface roughness of Ni, Ni–pumice and Ni–SiC coatings electrodeposited at 0.77 A dm^{-2} and 300 rpm was 0.19, 1.79 and 1.1 μm respectively. The roughness data clearly indicated the rough nature of the Ni–pumice coating. The higher roughness of Ni–pumice coating was due to the incorporation of coarser particles. However, roughness may be further reduced by eliminating larger pumice particles.

Fig. 7 shows the plots of microhardness vs. current density for Ni–pumice coatings electrodeposited at various magnetic stirring rates (rpm). A maximum microhardness of ~540 HK was exhibited by composite coating electrodeposited at an applied current density of 0.77 A dm^{-2}. This may be attributed to the higher area fraction of particles (23%) in the matrix. Interestingly, irrespective of the rpm used, lower microhardness values were obtained at higher current density. This is due to the fact that the rate of Ni deposition is higher at higher current density which results in higher rate of metal deposition and the chance entrapment of pumice particle is less. The dispersion of ceramic particles in the nickel matrix increases the microhardness of the coatings by two hardening mechanisms: (i) dispersion strengthening of coating and (ii) the dispersion of particles can cause grain size refinement of the nickel matrix by reducing the average grain size. The observed trend of decreased microhardness with increasing applied current density may be attributed to the increased grain size of nickel as evident from the XRD studies of Ni–pumice coatings (Section 3.2.1). The observed trend in microhardness with increasing current density is in accordance with Hall–Petch relationship. The Ni–SiC coating electrodeposited at the optimized electrodeposition conditions of 0.77 A dm^{-2} and 300 rpm exhibited a microhardness of 523 HK.

Table 2
Values of Rietveld refined parameters for pumice powder.

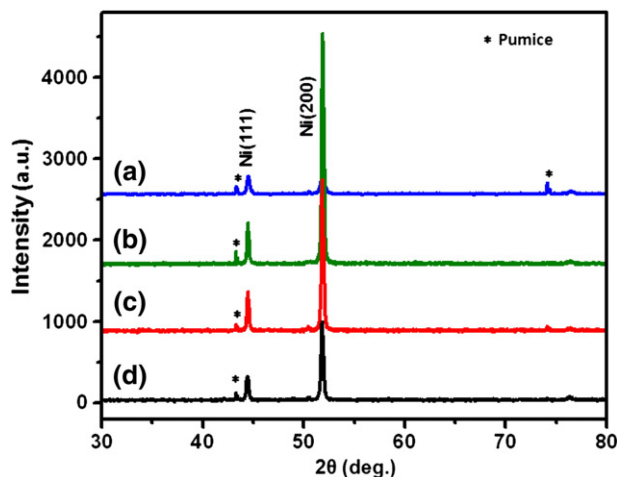| Structure	I	II	III	IV	V
Phase name	Corundum	Quartz low	Moganite	Mullite	Coesite
R-Bragg	98.786	99.093	98.740	99.105	98.473
Space group	R-3̄cH	P3₂21	I12/a1	Pbam	C12/c1
Cell mass	611.768	264.508	721.009	316.808	961.346
Cell volume (Å³)	256.086	112.893	436.231	167.786	523.933
Rietveld (wt.%)	4.641	10.976	5.937	33.267	45.179
Crystallite size (nm)	95.9	175.7	162.5	117.9	38.7
Crystal density (g cm^{-3})	3.967	3.891	2.745	3.135	3.047
Lattice parameters	a (Å) = 4.789	a (Å) = 4.911	a (Å) = 8.495	a (Å) = 7.557	a (Å) = 7.025
	c (Å) = 12.915	c (Å) = 5.404	b (Å) = 4.768	b (Å) = 7.695	b (Å) = 12.116
			c (Å) = 10.768	c (Å) = 2.885	c (Å) = 7.051
			β (°) = 89.499		β (°) = 119.203

Fig. 4. The XRD patterns of Ni–pumice coatings electrodeposited at 300 rpm and different current densities (a) 0.77, (b) 1.55, (c) 3.1 and (d) 4.65 A dm^{-2}.

Table 4 shows the wear volume loss, coefficient of friction, and wear rates for pure Ni, Ni–pumice and Ni–SiC coatings electrodeposited at 0.77 A dm^{-2} and 300 rpm. Fig. 8 shows the plots of wear loss vs. sliding time (Fig. 8a) and coefficient of friction vs. sliding time (Fig. 8b) for pure nickel, Ni–pumice and Ni–SiC coatings. Ni–pumice coating showed the minimum wear loss (~10 μm for 1500 s) compared to plain nickel and Ni–SiC electroplated and tested under similar conditions (Fig. 8). All the three coatings exhibited almost similar variations in coefficient of friction (Fig. 8b). The improved wear resistance of Ni–pumice coating may be attributed to the abrasive nature of the alumina and mullite ceramic particles present in the pumice powder. The wear rate of all the coatings is in the order of 10^{-5} and 10^{-6} mm^3/m. These values indicate that all the coatings have undergone mild adhesive wear of a burnishing type [24]. Although the major wear mechanism was the same for all the three coatings, the wear rates were significantly different and the wear rate was the lowest for Ni–pumice coating. There was a tenfold increase in wear resistance of Ni by the incorporation of pumice particles. The lower wear coefficient values obtained for Ni–pumice and Ni–SiC agree well with the values reported for Ni–SiC [25].

In the case of Ni–pumice coating transferred disk, due to the low wear loss of Ni–pumice coating, very little material was transferred to the disk (Fig. 9a) and more material transfer was observed with plain nickel (Fig. 9b). Usually the material transfer from the pin to the disk during wear testing is studied by recording the Raman spectra of the wear track. The Raman spectrum of the wear track of Ni–pumice coating showed peaks at 240, 300, 410 and 650 cm^{-1}. The Raman peaks observed at 300 and 410 cm^{-1} correspond to mullite phase [26] and the one at 240 cm^{-1} corresponds to moganite phase [27]. The Raman peak at 650 cm^{-1} corresponds to corundum (α-Al$_2$O$_3$) [28]. This clearly proved the transfer of pumice particles from the coated pin onto the disk during wear test.

3.2.3. Texture development

Fig. 10 shows the texture evolution in the electrodeposited Ni and Ni–pumice coatings in terms of experimentally measured {200} pole figures (CPFs) and normal direction inverse pole figures (ND IPFs). As per the specimen scheme used for X-ray texture measurement, normal direction at the center of these CPFs coincides with the physical growth direction of the electrodeposited coatings. Similarly, in the ND IPFs, the growth direction was plotted in the frame work of three principal crystal coordinates for cubic crystal system, <100>, <110> and <111>. In the case of the electrodeposited Ni–pumice composite coating, the {200} CPF showed strong intensity maxima at the center with a maximum spread of ~10°. Similarly, ND IPF for this coating exhibited strong intensity maxima only near <001> direction which again spreads maximum up to ~10°. This implied that most of the grains in this coating were oriented such that their <001> crystallographic direction were parallel to the specimen normal i.e. physical growth direction for the coating. Exactly similar observations were made in the case of electrodeposited Ni coating without any reinforcing phase. Both the {200} CPF and ND IPF showed strong intensity maxima close to the center and near <001> direction, respectively which indicated growth direction of the coating being parallel to <100> crystallographic direction.

Such strong <001>∥ growth direction texture for electrodeposited Ni coatings was earlier reported by Nielsen et al. [29]. Interestingly, the overall intensity of texture development was slightly stronger for the Ni–pumice composite coating than plain Ni coating which was quite evident from the intensity levels given alongside the pole figures and ND
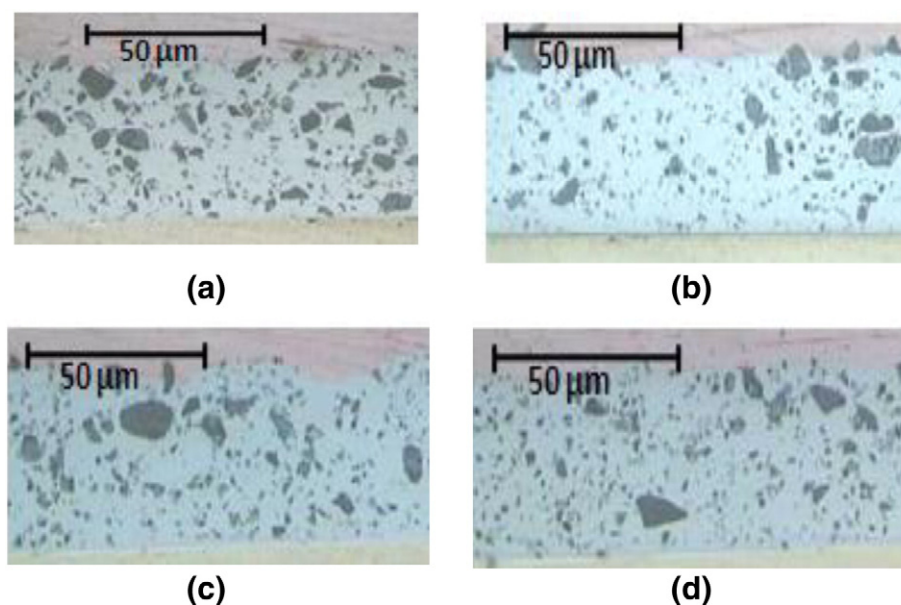

(a)

(b)

(c)

(d)

Fig. 5. Cross-sectional optical micrographs of Ni–pumice coatings electrodeposited at 300 rpm and current densities (a) 0.77, (b) 1.55, (c) 3.1 and (d) 4.65 A dm^{-2}.
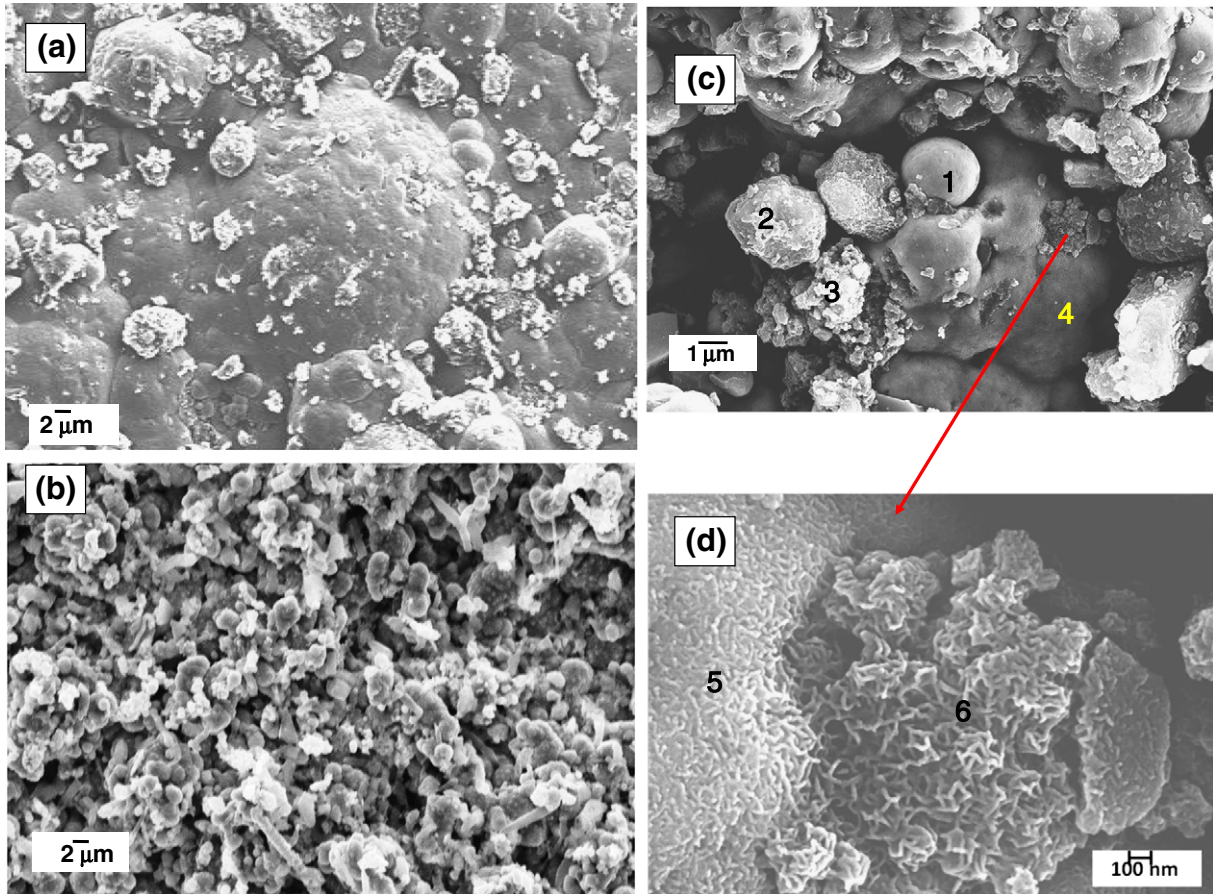
Fig. 6. Surface FESEM images of coatings electrodeposited at 0.77 A dm^{-2} and 300 rpm (a) Ni–pumice and (b) Ni–SiC composite coatings (3000 × magnification) and (c) and (d) FESEM images of Ni–pumice coating on which EDAX was performed.

IPFs. The CPFs as well as IPFs for these two coatings were expressed in the same intensity levels for comparing their relative texture strengths.

The most significant effect of texture evolution in the electrodeposited Ni and Ni–pumice coatings can be realized in their respective response toward mechanical loading. This is to say, the crystallographic orientation of these coatings with respect to the external loading directions might interfere apart from the other effects e.g. matrix grain size, size and volume fraction of secondary phase as has been explicitly reported by various researchers [30–34]. The strong texture evolution in these coatings might affect respective hardness values and subsequently modify tribological performances (wear rate and coefficient of friction) of the coatings. As has been discussed both the pure Ni and Ni–pumice coatings were characterized by strong <001>∥ growth direction type texture. With respect to the mechanical loading (e.g. indentation) along the normal to the coating surface, the stress direction obviously became parallel to <001> direction for most of the grains. This <001> direction is usually considered to be a "soft" direction under indentation for fcc materials while <111>∥ loading direction is taken as 'hard' direction [32–34]. Thus, in addition to other factors, the texture factor may somewhat contribute to the wear rate for the two coatings.

Furthermore, from a crystallographic texture point of view, it is expected that the hardness would be lower and correspondingly, wear rate would be higher for the Ni–pumice coating compared to the pure Ni-coating. This means, since the former coating showed higher strength of texture than the later meaning that affluent numbers of grains for the former coating are favorably oriented along the 'soft' direction under indentation or wear pin. This is exactly the opposite of

Table 3
EDAX data recorded on various spots on the surface of Ni–pumice coating (Fig. 6c and d).

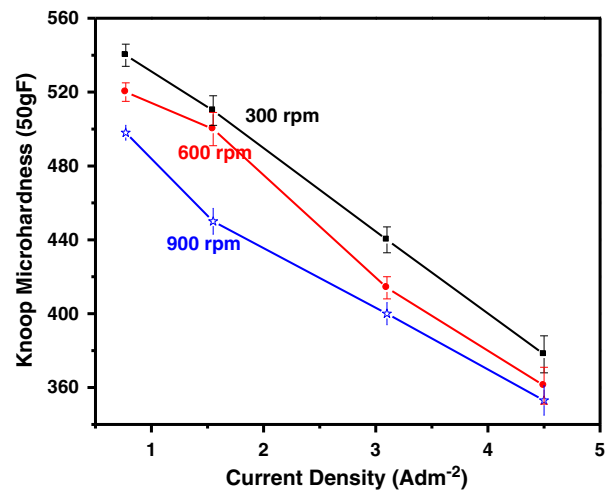| Element	Weight %					
	Spot 1	Spot 2	Spot 3	Spot 4	Spot 5	Spot 6
O	15.11	45.49	21.72	3.59	3.65	15.07
Al	4.98	16.16	6.20	3.01	0.94	4.95
Si	5.78	13.77	10.23	1.51	0.77	5.82
Ni	74.13	24.59	61.85	93.33	94.63	74.16

Fig. 7. Plots of Knoop microhardness vs. applied current density of Ni–pumice coatings electrodeposited at different magnetic agitation speeds.

Table 4
Wear test data of Ni, Ni–SiC and Ni–pumice coatings.

Coating	Coefficient of friction	Wear volume loss (mm³)	Wear coefficient	Wear rate (mm³/m)
Pure Ni	0.789	0.1264	1.39×10^{-5}	5.59×10^{-5}
Ni–SiC	0.753	0.0303	6.97×10^{-6}	1.34×10^{-5}
Ni–pumice	0.712	0.0131	3.14×10^{-6}	5.82×10^{-6}

what had been noticed in the present study with Fig. 8 showing wear loss with time. Thus we can conclude that the texture evolution is possibly not the strongest deciding factor for the improved properties of Ni–pumice coatings [32,34].

3.2.4. Oxidation resistance of Ni–pumice coatings

In the literature, the reported oxidation resistance experiments involved the determination of mass change as a function of temperature. Since the microhardness of the coatings deteriorate with heat treatment, the variation of microhardness with heat treatment was studied in the present work. Fig. 11 shows the plots of microhardness vs. heat treatment temperature for Ni, Ni–pumice and Ni–SiC. Ni–pumice composite coating exhibited higher microhardness values irrespective of the heat treatment temperatures compared to plain nickel indicating a higher oxidation resistance for Ni–pumice. The microhardness was higher for Ni–pumice coating up to 500 °C, and after this temperature the microhardness values were similar to that of Ni–SiC coating. The improved oxidation resistance of Ni–pumice may be attributed to the inhibition of the predominant outward diffusion of Ni along NiO grain boundaries by the segregated particles [35].

The isothermal oxidation kinetics of the as-deposited Ni, Ni–SiC and Ni–pumice composite coatings at 800 °C for 30 h with intervals of 5 h is illustrated in Fig. 12, which shows improved oxidation resistance of Ni–pumice composite until 20 h heat treatment when compared to Ni and Ni–SiC composite coatings. After 20 h, the oxidation resistance of Ni–pumice and Ni–SiC coatings was similar and better than plain Ni coating. This clearly showed improved oxidation resistance of Ni–pumice coating over plain nickel. Interestingly, the oxidation resistance of Ni–pumice coating was similar to Ni–SiC coating and thus Ni–pumice can be a potential candidate to Ni–SiC.

4. Conclusions

Commercially available inexpensive pumice stone (15 times cheaper than SiC) was crushed and subjected for ball milling to obtain pumice particles that were suitable for electrodeposition. Ni–pumice composite coating was electrodeposited from a nickel sulfamate bath containing pumice particles. In general, the microhardness values of Ni–pumice coatings decreased with increased applied current density and coatings
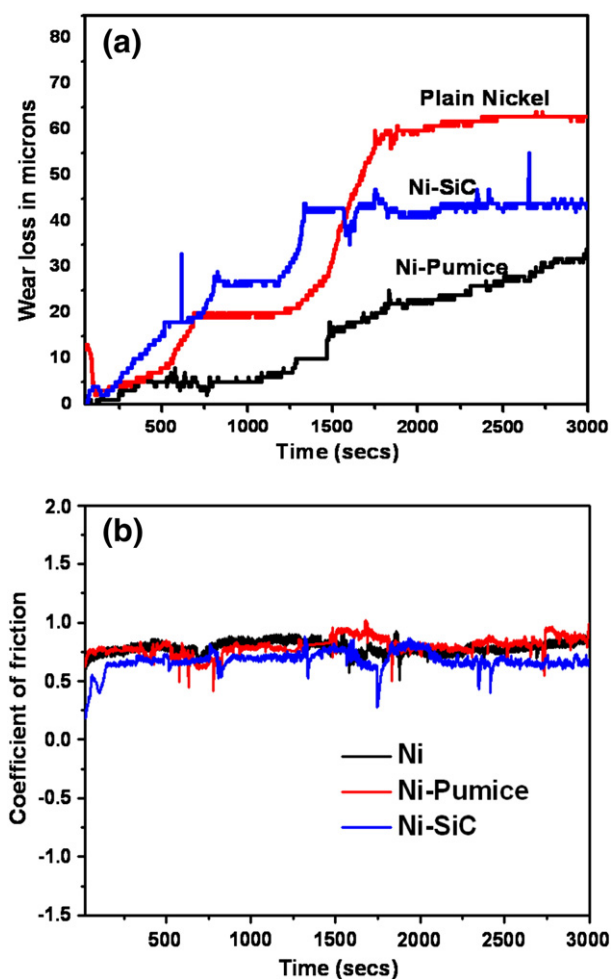

Fig. 8. (a) Plots of wear loss vs. sliding time and (b) coefficient of friction vs. sliding time for electrodeposited Ni, Ni–SiC and Ni–pumice coatings.
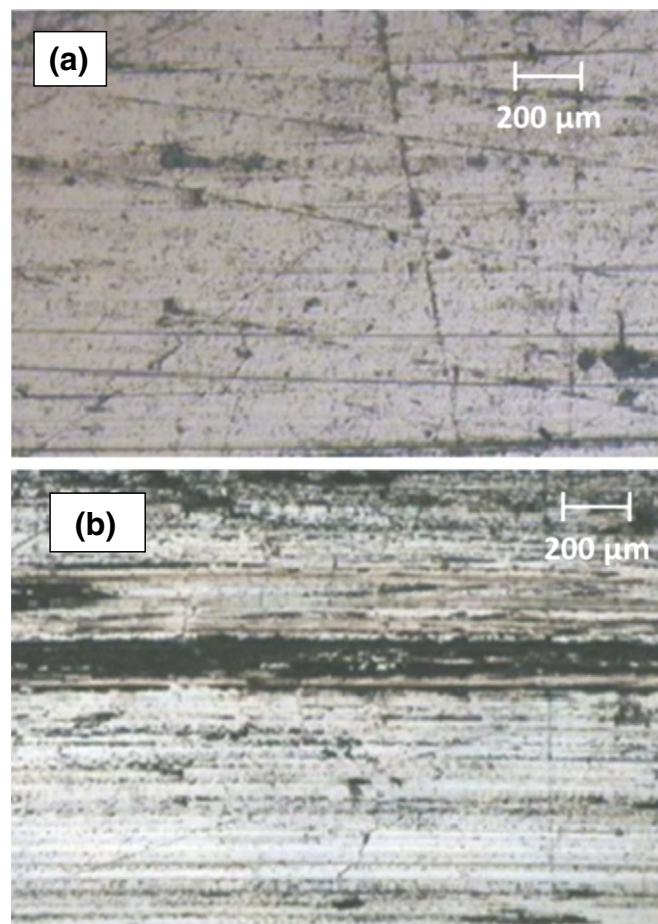

Fig. 9. Optical micrographs of wear tracks on disks corresponding to (a) Ni–pumice coatings and (b) Ni coatings.
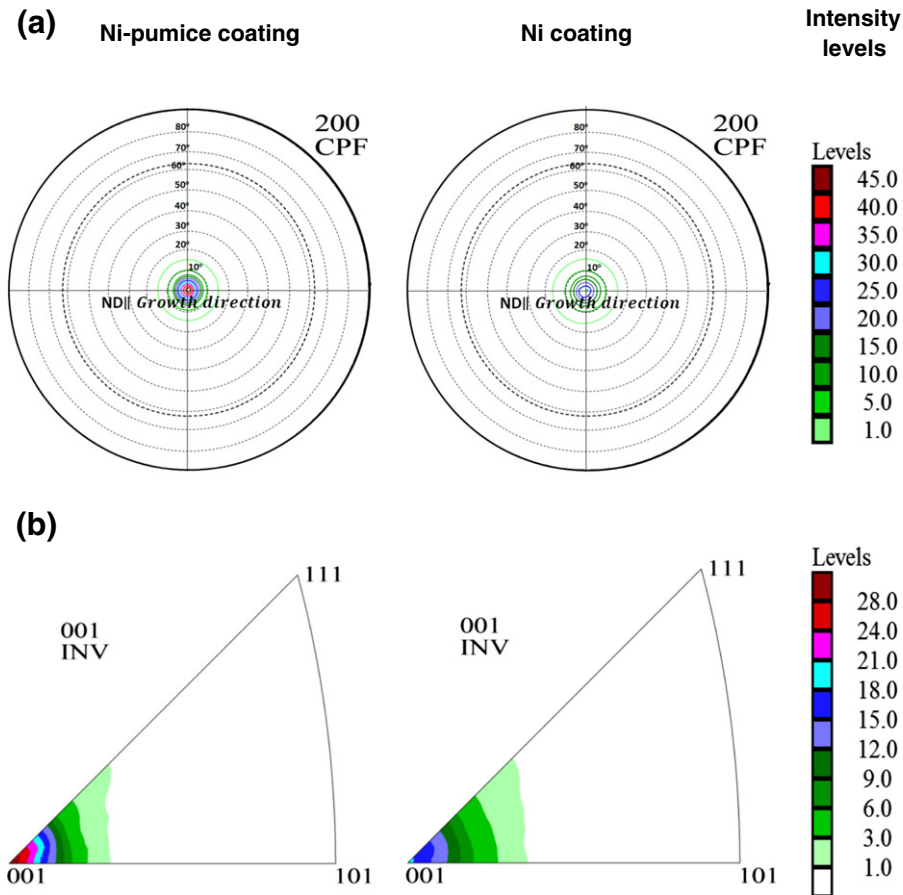
Fig. 10. Texture evolution in the electrodeposited Ni composite coating (left) and electrodeposited Ni coating (right) in terms of (a) {200} CPFs and (b) ND IPFs. Intensity levels are given alongside.

electrodeposited at 300 rpm yielded higher microhardness values. Irrespective of the current density used for electrodeposition, larger pumice particles were electrodeposited at lower magnetic agitation speed. The overall intensity of texture development was slightly stronger for the Ni–pumice composite coating compared to plain Ni coating and the texture evolution is possibly not the strongest deciding factor for the enhanced properties of Ni–pumice coatings. The wear and oxidation resistance of Ni–pumice coating was commensurate with that of Ni–SiC coating electrodeposited under similar conditions. This study clearly demonstrated pumice to be a potential candidate material for imparting improved microhardness, wear and oxidation resistant properties to the electrodeposited Ni-composite coatings. Thus electrodeposited Ni–pumice coating may be a cost-effective coating which can be an alternative to the traditional Ni–SiC coating, which is widely used for coating trochoids of Wankel engines.
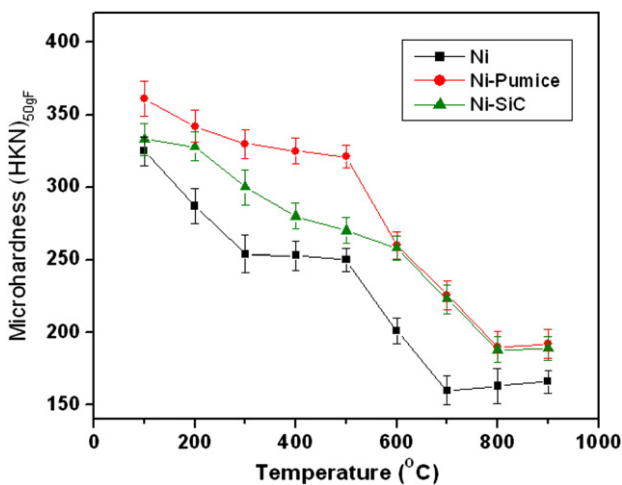

Fig. 11. Plots of microhardness vs. heat treatment temperatures for Ni, Ni–pumice and Ni–SiC coatings.
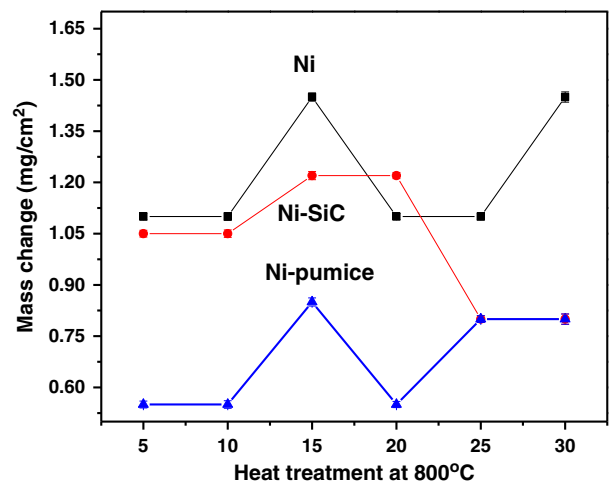

Fig. 12. Kinetics of isothermal oxidation in air at 800 °C for Ni, Ni–SiC and Ni–pumice electrodeposited composites.

Conflict of interest

The authors have no conflict of interest.

Acknowledgments

References

[1] J.R. Roos, J.P. Celis, J. Fransaer, C. Buelens, J. Metall. 42 (1990) 60–63.
[2] J. Fransaer, J.P. Celis, J.R. Roos, J. Electrochem. Soc. 139 (1992) 413–425.
[3] A. Hovestad, L.J.J. Janssen, J. Appl. Electrochem. 40 (1995) 519–527.
[4] B. Szczygiel, M. Kolodziej, Electrochim. Acta 50 (2005) 4188–4195.
[5] M.R. Vaezi, S.K. Sadrnezhaad, Colloids Surf. A Physicochem. Eng. Asp. 315 (2008) 176–182.
[6] http://en.wikipedia.org/wiki/Wankel_engine .
[7] M.A. Khazrayie, A.R.S. Aghdam, Trans. Nonferrous Met. Soc. China 20 (2010) 1017–1023.
[8] S.T. Aruna, V.K. William Grips, K.S. Rajam, J. Appl. Electrochem. 40 (2010) 2161–2169.
[9] W. Wang, F.-Y. Hou, H. Wang, H.-T. Guo, Scr. Mater. 53 (2005) 613–618.
[10] S.T. Aruna, C.N. Bindu, V. Ezhil Selvi, V.K. William Grips, K.S. Rajam, Surf. Coat. Technol. 200 (2006) 6871–6880.
[11] D.E. Rusu, P. Cojocaru, L. Magagnin, C. Gheorghies, G. Cârâc, J. Optoelectron. Adv. Mater. 12 (2010) 2419–2422.
[12] Y.-J. Xue, D. Zhu, F. Zhao, J. Mater. Sci. 39 (2004) 4063–4066.
[13] Y.S. Jeon, J.Y. Byun, T.S. Oh, J. Phys. Chem. Solids 69 (2008) 1391–1394.
[14] T. Tsubota, T. Shunsuke, T. Ishida, M. Nagata, M. Yasumichi, Diamond Relat. Mater. 14 (2005) 608–612.
[15] A. Kantepozidou, C. Kiparissides, F. Kotzia, C. Kollia, N. Spyrellis, J. Mater. Sci. 31 (1996) 1175–1181.
[16] F. Akbal, N. Akdemir, A.N. Onar, Talanta 53 (2000) 131–135.
[17] M. Yavuz, F. Godea, E. Pehlivan, S. Ozmert, Y.C. Sharma, Chem. Eng. J. 137 (2008) 453–461.
[18] A.N. Onar, N. Balkaya, T. Akyuz, Environ. Technol. 17 (1996) 207–213.
[19] S.T. Aruna, V.K. William Grips, S. Latha, M. Muni Prakash, Indian Patent no., 0160NF2013 filed 13/09/2013.
[20] H.M. Rietveld, J. Appl. Crystallogr. 2 (1969) 65–71.
[21] S.T. Aruna, V.K. William Grips, K.S. Rajam, J. Alloys Compd. 468 (2009) 546–552.
[22] J.X. Kan, W.Z. Zhao, G.F. Zhang, Surf. Coat. Technol. 203 (2009) 1815–1818.
[23] D. Thiemig, A. Bund, J.B. Talbot, Electrochim. Acta 54 (2009) 2491–2498.
[24] E. Rabinowicz, Wear 100 (1984) 533–542.
[25] M. Srivastava, V.K. William Grips, K.S. Rajam, Appl. Surf. Sci. 253 (2007) 3814–3824.
[26] Ph. Colomban, J. Mater. Sci. 24 (1989) 3011–3020.
[27] K.J. Kingma, R.J. Hemley, Am. Mineral. 79 (1994) 269–273.
[28] S.P.S. Porto, R.S. Krishnan, J. Chem. Phys. 47 (1967) 1009–1012.
[29] C.B. Nielsen, A. Horsewell, M.J.L. Ostergard, J. Appl. Electrochem. 27 (1997) 839–845.
[30] C. Cheung, F. Djuanda, U. Erb, G. Palumbo, Nanostruct. Mater. 5 (1995) 513–523.
[31] H.S. Cho, K.J. Hemker, K. Lian, J. Goettert, G. Dirras, Sensors Actuators A Phys. 103 (2003) 59–63.
[32] F. Ebrahimi, G.R. Bourne, M.S. Kelly, T.E. Matthews, Nanostruct. Mater. 11 (1999) 343–350.
[33] K. Schüler, B. Philippi, M. Weinmann, V.M. Marx, H. Vehoff, Acta Mater. 61 (2013) 3945–3955.
[34] A.F. Zimmerman, G. Palumbo, K.T. Aust, U. Erb, Mater. Sci. Eng. A 328 (2002) 137–146.
[35] Y.B. Zhou, J.F. Sun, S.C. Wang, H.J. Zhang, Corros. Sci. 63 (2012) 351–357.